THz Imaging Using Uncooled Wideband Direct Detection Focal Plane Arrays

Sven van Berkel, *Student Member, IEEE*, Ozan Yurduseven, *Student Member, IEEE*, Angelo Freni, *Senior Member, IEEE*, Andrea Neto, *Fellow, IEEE*, and Nuria Llombart, *Senior Member, IEEE*

(Invited Paper)

***Abstract*—In millimeter and submillimeter-wave radiometric imaging systems, a persistent goal is the increase in the speed of acquisition of the image while maintaining a high sensitivity. Typically, the highest sensitivity is achieved by cryogenically cooling the detectors, specifically in astronomical applications. However, for the purpose of low-cost imaging applications, it is desirable to operate at room temperature. Without cryogenically cooling, the electronic noise introduced by the detectors becomes dominant, making the detectors less sensitive. Resorting to detection architectures containing amplification circuitry might be impractical for implementation in large focal plane arrays (FPAs) fabricated in integrated technologies. This contribution derives the focal plane architecture that maximizes the imaging speed of radiometers operating at room temperature without using any amplification circuitry. It is shown that in such scenario a practical image acquisition speed can still be achieved when a very broad portion of the THz-band is exploited. Ultimately, the imaging speed is maximized when the FPA is undersampled, implying a tradeoff in the size of the optics. The analysis is substantiated by a case study with recently developed wideband leaky lens antenna feeds operating from 200 to 600 GHz.**

***Index Terms*—Direct detection, focal plane arrays (FPAs), leaky lens antennas, passive imaging, radiometry, wideband antennas.**

I. Introduction

In MICROWAVE and millimeter wave radiometry, much effort has been made in the development of efficient amplification circuitry and tunable coherent sources for large arrays. However, in the submillimeter regime of the electromagnetic spectrum, i.e., from 300 GHz and above, the design of active circuitry is still considered to be a challenging task [1]. Detection at submillimeter-wave frequencies would then preferably be performed incoherently. In this contribution, we focus on incoherent detection (i.e., direct detection) architectures in the absence of amplifiers or mixers. Such architectures require a quasi-optical system with lenses or reflectors in combination with a focal plane array (FPA) in order to generate the image. Incoherent detectors have the advantage of an easier read-out and a low power consumption. This enables the fabrication of a large number of detectors in the FPA when using integrated solutions such as CMOS [2] or superconducting technologies [3], [4]. In [5], direct detectors are roughly classified into three categories: thermal detection, cryogenically cooled detectors based on superconducting technologies, and rectifying diodes. The first passive (mm-wave) imaging systems, consisting of diodes operating around 90 GHz [6] and bolometers [7], only had few detectors, resulting in a large image acquisition time and/or a small field-of-view (FoV). Since then, in order to achieve a sufficient signal-to-noise ratio (SNR) for fast frame rates and extreme sensitivities, FPAs have been cryogenically cooled and fabricated in integrated technologies to decrease the electronic/thermal noise contributions and increase the FoV [3], [4], [8]–[10]. Ultimately, the SNR is limited by the (thermal) fluctuations of the signal itself, i.e., background-noise limited.

A cornerstone in the dimensioning and characterization of direct detection systems that are based on absorbers or background-noise limited detectors is presented in [11], where different FPA configurations are compared in terms of imaging speed and SNR. However, [11] is limited in its scope since it focuses only on cooled detectors and, more importantly, the effect of bandwidth is not included. Cryogenically cooling the detectors is expensive and results in a bulky system; for the purpose of low-cost imaging applications, it is desired to have a large integrated FPA operating at room temperature. In this scenario, the electronic noise introduced by the detectors is much higher such that none of the existing uncooled direct detectors operate near the background-noise limit [12]; the current state-of-the-art uncooled passive submillimeter-wave imagers [2], [13]–[19] are insufficiently sensitive to operate without actively illuminating the source of interest.

This contribution derives a focal plane architecture, for antenna-coupled direct detectors, that is able to provide a practical sensitivity and imaging speed (e.g., 1 K [20] at near real-time

Manuscript received June 12, 2017; revised July 21, 2017; accepted July 24, 2017. Date of publication August 25, 2017; date of current version September 13, 2017. This work was supported by the Dutch Technology Foundation STW (Project Terahertz silicon-Integrated CAMera, TiCAM, 13325), which is part of the Netherlands Organization for Scientific Research (NWO), and which is partly funded by the Ministry of Economic Affairs. The work of A. Neto was supported by European Research Council Consolidator Grant AAATSI 278794. The work of N. Llombart was supported by the European Research Council for the starting Grant LAA-THz-CC 639749. *(Corresponding author: Sven van Berkel.)*

S. van Berkel, O. Yurduseven, A. Neto, and N. Llombart are with the THz Sensing Group, Delft University of Technology, Delft 2628 CD, The Netherlands (e-mail: s.l.vanberkel@tudelft.nl; O.Yurduseven@tudelft.nl; A.Neto@tudelft.nl; n.llombartjuan@tudelft.nl).

A. Freni is with the Department of Information Engineering, University of Florence, 50139 Florence, Italy (e-mail: angelo.freni@unifi.it).

Color versions of one or more of the figures in this paper are available online at http://ieeexplore.ieee.org.

Digital Object Identifier 10.1109/TTHZ.2017.2736338

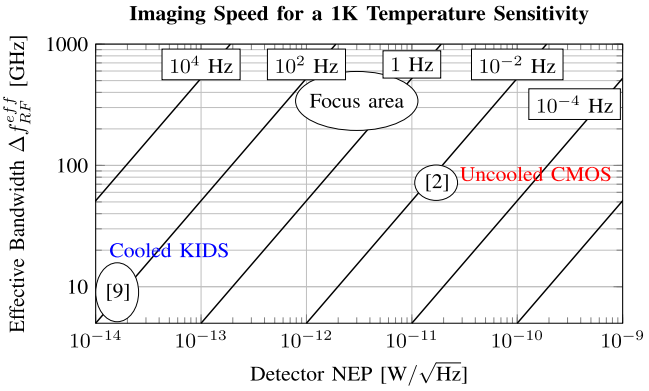

Fig. 1. Imaging speed for 1 K temperature sensitivity (1) for state-of-the-art passive imagers with more than 1k-pixels and a measured temperature sensitivity: Cryogenically cooled kinetic inductance bolometers in [9] and uncooled CMOS detectors in [2]. Furthermore, the focus area of this work is indicated.

refresh rates for security screening) without cooling, amplification, or active illumination. As will be derived in Section II-A, the temperature sensitivity, also referred to as the noise equivalent temperature difference (NETD), of a direct detector after $\tau_{\rm int}$ seconds of integration and without any preamplification can be expressed as

$$\text{NETD} = \frac{\text{NEP}}{k_B \Delta f_{\rm RF}^{\rm eff} \sqrt{2\tau_{\rm int}}} \tag{1}$$

with $k_B = 1.38 \times 10^{-23}$ m^2 kg s^{-2} K^{-1} being Boltzmann's constant, $\Delta f_{\rm RF}^{\rm eff}$ is the effective bandwidth[1] and NEP is the noise equivalent power for a 1 Hz postdetection bandwidth, $\Delta f_{\rm PD}$.[2] As is clear from (1), the crucial aspect in achieving a practical NETD is the utilization of detectors characterized by a low NEP that are matched over a broad portion of the THz-spectrum to an antenna. To illustrate this, Fig. 1 shows the imaging speed as $1/\tau_{\rm int}$ versus $\Delta f_{\rm RF}^{\rm eff}$ and NEP such that the minimum practical temperature sensitivity of 1 K in (1) is achieved. Nowadays, detectors suitable for array implementation have been shown with room temperature NEPs as low as 12.6 pW$/\sqrt{\text{Hz}}$ in CMOS technologies [13], [22], 2.4 pW$/\sqrt{\text{Hz}}$ for commercially available zero-bias Schottky-barrier diodes [23] and even 0.48 pW$/\sqrt{\text{Hz}}$ in III-V technologies [24]. Therefore, with this order of magnitude in NEP, one can utilize a large operational bandwidth to achieve a practical sensitivity and imaging speed. Novel integrated wideband antenna concepts that can be exploited in this kind of scenario are connected arrays [25] or leaky lens antennas [26] which have been recently developed. The focus area of this work is indicated in Fig. 1, the work describes the FPA design steps to maximize the effective bandwidth for uncooled FPAs. Of course, an important condition to facilitate the efficient use of a large operational bandwidth is a wideband impedance match of the antenna feeds with the detector. When the antenna and detector are codesigned, an impedance match over a relative bandwidth of $\nu = \frac{f_{\rm max}}{f_{\rm min}} = 3$ can be achieved [27].

[1]Effective bandwidth is defined as the average optical efficiency, $\bar{\eta}_{\rm opt}$, times the absolute bandwidth, $\Delta f_{\rm RF}$: $\Delta f_{\rm RF}^{\rm eff} = \bar{\eta}_{\rm opt} \Delta f_{\rm RF}$ (See Section II-A)

[2]A 1 Hz postdetection bandwidth is equivalent to 0.5 s of detector integration time; $\Delta f_{\rm PD} = \frac{1}{2\tau_{\rm int}}$ [21].

A. State-of-the-Art of > 1k-Pixel FPAs

A persistent goal in submillimeter-wave imaging systems is to increase the FoV. This can be achieved by fabricating large integrated FPAs. Passive submillimeter-wave FPAs with 1 kilopixels or more have been demonstrated in [2], [3], [9], [16]–[19]. For the purpose of astronomical observations, the highest sensitivity is achieved by cryogenically cooling the FPA of antenna-coupled kinetic inductance detectors in [3], where the detectors are background-noise limited with a measured NEP $= 3 \cdot 10^{-19}$ W$/\sqrt{\text{Hz}}$. Measurements of the temperature sensitivity, using a calibrated black body source, have been done for [2] and [9]. For more commercial applications, a cooled FPA of KIDs operating at 7 K has been proposed in [9]. This FPA is detector-noise limited, with a measured NETD between 110 and 190 mK for 0.5 s of detector integration time with a parallel read-out of the detectors. The optical efficiencies presented in [9] suggest an effective bandwidth around 10 GHz.[3] The *uncooled* FPA in [2], based on 32×32 CMOS ring antennas, has sensitivity measurements presented in [28], yielding a 20.86 K sensitivity for an integration time of 5.7 min with a consecutive read-out of the detectors.[4] The measured noise, integrated over a 500 kHz postdetection bandwidth, is reported to be 12 nW.[5] Other large uncooled FPAs, without sensitivity measurements, are [16]–[19] which are based on microbolometers and heterostructure backward diodes.

The required imaging speeds of [2] and [9] to achieve a 1 K temperature sensitivity (1) are compared in Fig. 1, yielding a 55–165 Hz refresh rate for [9] and a $7 \cdot 10^{-3}$ Hz refresh rate[6] for [2].

The paper is organized as follows. In Section II, the theory used throughout this work is derived by following an electromagnetic approach assuming ideal and uniformly illuminated circular feeds placed in a square array in the focal plane of a symmetric quasi-optical system, as shown in Fig. 2. Figures of merit such as sensitivity, imaging speed, and noise equivalent power are introduced, which are used to analyze the optimal FPA configuration in terms of imaging speed in Section III and resolution in Section IV. In Section V, the analysis is substantiated by evaluating the imaging speed of leaky lens antennas operating from 200 to 600 GHz.

II. Quasi-Optical Radiometric System

Radiometry is the primary tool used to characterize the electromagnetic power spectrum of emission due to sources distributed in space. The key observable parameter is the spectral brightness distribution, $B(f, \Omega)$, of the source that is defined over a source solid angle Ω_S, with a temperature distribution $T_S(\Omega)$, as is shown in Fig. 2. In fact, the spectral brightness

[3]Using (1), the theoretically estimated NEP $= 1.6 \cdot 10^{-14}$ W$/\sqrt{\text{Hz}}$ in [9] is verified.

[4]This integration time is obtained by averaging frames at 30 Hz during 5.7 min. Every frame contains 1024 pixels which are consecutively read out.

[5]Assuming a flat noise spectral density, the NEP can be obtained using NEP $= \frac{12 \text{ nW}}{\sqrt{500 \text{ kHz}}} = 17$ pW$/\sqrt{\text{Hz}}$[2].

[6]Since the pixels are consecutively read out, in 5.7 min (342 s) of frame averaging, every pixel is effectively integrated during $\tau_{\rm int} = \frac{342}{1024} = 0.334$ s.

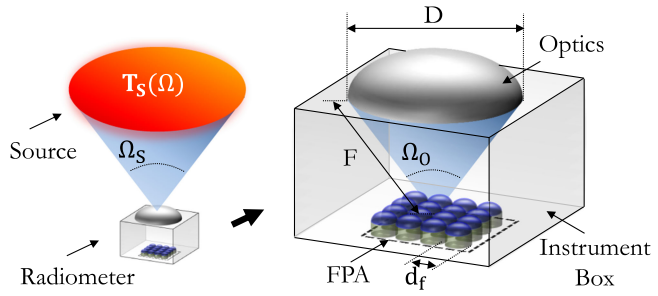

Fig. 2. Investigated quasi-optical system in the presence of an incoherent source with temperature distribution $T_S(\Omega)$ distributed over a source solid angle Ω_S. The radiometer consists of an FPA placed in an instrument box at a focal distance F from optics with diameter D that subtend the FPA with a solid angle of Ω_O. The investigated FPA is a square array containing antennas with diameter d_f.

distribution characterizes an incoherent source at temperature T and can be described by Planck's law in units of [W m^{-2} Sr^{-1} Hz^{-1}] [29]

$$B(f,\Omega)=\frac{f^2}{c^2}\frac{2hf}{e^{\frac{hf}{k_B T(\Omega)}}-1} \tag{2}$$

with f the frequency, $c=2.99\times10^8$ m/s the speed of light, and $h=6.626\times10^{-34}$ Js being Planck's constant. In the specific case that the radiometer is operating in the Rayleigh–Jeans region w.r.t. the source, i.e., when $hf \ll k_B T$ such as in a security scenario, a convenient approximation of the spectral brightness can be used

$$B(f,\Omega)|_{hf\ll k_B T}\approx B^{RJ}(f,\Omega)=\frac{f^2}{c^2}2k_B T(\Omega). \tag{3}$$

For sources with $T>270$ K and $f<1$ THz, the error in this approximation is less than 10%. It is worthwhile to mention that in Wien's limit, i.e., when $hf \gg k_B T$, the spectral brightness can be approximated using $(e^{\frac{hf}{k_B T}}-1)^{-1}\approx e^{-\frac{hf}{k_B T}}$; this term decreases exponentially with frequency and therefore only the lowest frequencies in the band contribute to the imaging speed. This implies that utilizing a large operational bandwidth is not very beneficial to increase the SNR when the radiometer is operating in Wien's limit w.r.t. the source such as is the case for deep-space sensing. Accordingly, optimal FPA configurations in Wien's limit can be studied as in [11]. In the rest of this paper, it is assumed that the radiometer is operating in the Rayleigh–Jeans limit (3) w.r.t. the source. A simplified configuration of the complex optics of a radiometer is shown in Fig. 2. In this configuration, antenna feeds are placed in a square FPA with an interelement spacing of d_f (in both directions) at a focal distance of F from the optics with a diameter of D ($F_\# = F/D$). The optics are assumed to be characterized by large $F_\#$ and subtend the FPA with a solid angle of Ω_O. In order to generalize the analysis, ideal antenna feeds are initially assumed to be characterized by uniformly illuminated circular apertures. Moreover, the efficiency of each of the antenna feeds and associated intensity patterns after the optics are assumed to be the same for all FPA elements, apart from the pointing angle. The feed apertures have the same diameter as the interfeed spacing d_f. The array is placed in an uncooled instrument box.

A. Imaging Speed

For direct detection schemes, the SNR, after $\tau_{\rm int}$ seconds of detector integration, can be expressed as [7], [21], [30]

$$\text{SNR}=\frac{P_a}{\text{NEP}\sqrt{\Delta f_{PD}}}=\frac{P_a}{\text{NEP}}\sqrt{2\tau_{\rm int}} \tag{4}$$

where P_a is the average power accepted by the detector during the integration time interval $\tau_{\rm int}$. The expression of the SNR (4) follows from the NEP, which is defined as the average input power that is necessary to equate the root-mean-square noise power fluctuations when the postdetection bandwidth $\Delta f_{\rm PD}=1$ Hz and therefore making the SNR unity. The image acquisition time τ_i is typically larger than the detector integration time $\tau_{\rm int}$ if one has fewer detectors $N_{\rm det}$ operating simultaneously than the number of pixels in the desired FoV, $N_{\rm pix}$. In that case $\tau_i=N_t\tau_{\rm int}$ with $N_t=\frac{N_{\rm pix}}{N_{\rm det}}$ defined as an integration time penalty to form a single image in τ_i seconds. This illustrates the great efforts that are done to fabricate large FPAs.

The average received power, during the detector integration time interval, from an incoherent source by the nth single polarized antenna feed P_a^n can be expressed as an integration of the spectral brightness (2) over the operational bandwidth $\Delta f_{\rm RF}=f_{\max}-f_{\min}$ and over the source solid angle viewed and weighted by the effective area $A_{\rm eff}^O(f,\Omega)$ of the quasi-optical system

$$P_a^n=\frac{1}{2}\int_{f_{\min}}^{f_{\max}}\int_{\Omega_S}A_{\rm eff}^O(f,\Omega-\Omega_n)B(f,\Omega)d\Omega df. \tag{5}$$

Focusing on the on-axis element ($n=0$), the effective area of the quasi-optical system can be related to the directivity $D^O(f,\Omega)$; $A_{\rm eff}^O(f,\Omega)=\frac{c^2}{f^2}\frac{1}{4\pi}\eta_{\rm opt}(f)D^O(f,\Omega)$, where $\eta_{\rm opt}(f)=\eta_{\rm feed}(f)\eta_{\rm so}^{\Omega_O}(f)$ is the system's optical efficiency that is separated in a radiation efficiency of the feed $\eta_{\rm feed}(f)$, and spill-over efficiency w.r.t. the optics $\eta_{\rm so}^{\Omega_O}(f)$. The feed efficiencies are for example impedance matching and conductor-/dielectric losses, while $\eta_{\rm so}^{\Omega_O}(f)$ is a more significant term defining how well the antenna feed pattern is coupled to the angular region subtended by the optics Ω_O. The spill-over efficiency can be defined as

$$\eta_{\rm so}^{\Omega_O}(f)=\frac{\int^{\Omega_O}D^f(f,\Omega)d\Omega}{4\pi} \tag{6}$$

where $D^f(f,\Omega)$ is the directivity of the feed. In Fig. 3, the spill-over efficiency is shown as a function of the feed size, assuming large $F_\#$ and a uniformly illuminated circular aperture. It is evident that the spill-over efficiency, and therefore imaging speed, will be greatly affected by the choice of the feed size (which for simplicity corresponds to the interelement period in the FPA, i.e., *sampling*). For this reason, the spill-over efficiency will be the key parameter used in the analysis to derive the optimal sampling configuration. One should also note that a low spill-over efficiency also implies that the system can become sensitive to the thermal radiation coming from the instrument box. We assume that the instrument box, together with the quasi-optics, is kept at a stable temperature such that common calibration techniques can be applied. Substituting the effective area and

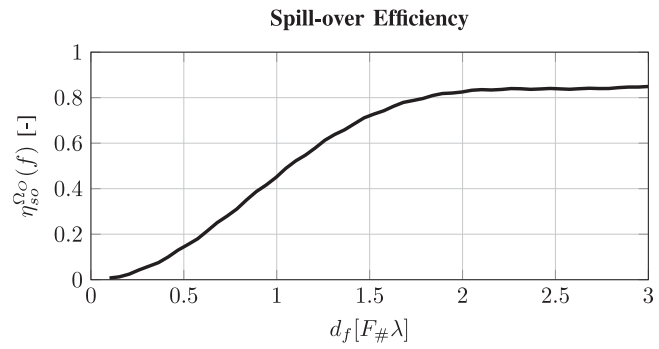

Fig. 3. Spill-over efficiency as a function of the feed size d_f, normalized to $F_\# = \frac{F}{D}$ and wavelength λ. The curve is evaluated using a uniformly illuminated circular feed that is placed in the focal plane of optics characterized with large $F_\#$.

the Rayleigh–Jeans approximation from (3) in (5) leads to

$$P_a = \frac{k_B}{4\pi}\int_{\Omega_S} T(\Omega)G_{\text{eff}}(\Omega)d\Omega \tag{7a}$$

$$G_{\text{eff}}(\Omega) = \int_{f_{\min}}^{f_{\max}} \eta_{\text{opt}}(f)D^O(f,\Omega)df. \tag{7b}$$

G_{eff}, the *effective gain pattern*, is obtained by weighting the spectral directivity by the optical efficiency of the quasi-optical system and by integrating the resulting term over the operational bandwidth.

A signal can be resolved by the system if the received power P_a (7a) integrated over time results in an SNR larger than 1 (4). In order to have a convenient way to compare the SNR for different FPA architectures, we make some assumptions in the evaluation of (7a). First, the source is considered to have an effective, constant, temperature $\bar{T}_S$ over the entire solid angle such that it can be removed from the integral over source solid angle. Second, an important condition of the presented analysis is that the sources are distributed over a large solid angle w.r.t. intensity patterns after the optics, such that the angular integration in (7a) over the spectral directivity in (7b) is approximately 4π. The average received power $\bar{P}_a$ by each antenna feed can now be written as (8a)

$$\bar{P}_a = k_B\bar{T}_S\bar{\eta}_{\text{opt}}\Delta f_{\text{RF}} \tag{8a}$$

$$\bar{\eta}_{\text{opt}} = \frac{1}{\Delta f_{\text{RF}}}\int_{f_{\min}}^{f_{\max}} \eta_{\text{opt}}(f)df. \tag{8b}$$

Here, we defined an average optical efficiency $\bar{\eta}_{\text{opt}}$. A convenient definition to characterize the performance of the quasi-optical system is its *effective bandwidth* $\Delta f_{\text{RF}}^{\text{eff}} = \bar{\eta}_{\text{opt}}\Delta f_{\text{RF}}$. This definition of effective bandwidth is used in Fig. 1.

Let us consider an incoherent source with an effective temperature of $\bar{T}_S$. A temperature difference ΔT in the incoherent source then results in a difference in average received power ΔP_a, according to $\bar{P}_a + \Delta P_a = k_B(\bar{T}_S + \Delta T)\bar{\eta}_{\text{opt}}\Delta f_{\text{RF}}$. The purpose of detector integration is to average the fluctuating received power over time in order to detect ΔP_a. Substituting $\Delta P_a = k_B\Delta T\bar{\eta}_{\text{opt}}\Delta f_{\text{RF}}$ in (4) and by forcing SNR $= 1$, we can solve for ΔT. This defines the sensitivity of the quasi-optical system as has been introduced in (1) [30]

$$\text{NETD} \triangleq \Delta T|_{\text{SNR}=1} = \frac{\text{NEP}}{k_B\bar{\eta}_{\text{opt}}\Delta f_{\text{RF}}\sqrt{2\tau_{\text{int}}}}. \tag{9}$$

One should be careful in interpreting the NEP and its impact on sensitivity. Usually, the NEP can be divided into two contributions; $\text{NEP}^2 = \text{NEP}_{\text{det}}^2 + \text{NEP}_b^2$. The detector noise NEP_{det} is intrinsic to the detector characteristics and strongly influenced by the read-out mechanism, while the background noise NEP_b is associated with the thermal fluctuations of the signals arriving at the input of the detector. For uncooled and fully passive systems, NEP_b is often a few orders of magnitude lower than NEP_{det} and can be neglected.[7] Rearranging (9) and substituting $\tau_{\text{int}} = \frac{\tau_i}{N_t}$ gives us an expression of the imaging speed s (10)

$$s = \frac{1}{\tau_i} = \left(\frac{\text{NETD}\cdot k_B\bar{\eta}_{\text{opt}}\Delta f_{\text{RF}}}{\text{NEP}}\right)^2\frac{2}{N_t} \tag{10}$$

Fig. 1, from the introduction, is generated using (10) as a function of $\Delta f_{\text{RF}}^{\text{eff}} = \bar{\eta}_{\text{opt}}\Delta f_{\text{RF}}$ and NEP, after fixing $N_t = 1$, and NETD $= 1$ K. When comparing two different configurations α and β, Griffin *et al.* [11] suggests focusing on the ratio in imaging speed (SR):

$$SR = \frac{s^\alpha}{s^\beta} = \left(\frac{\bar{\eta}_{\text{opt}}^\alpha\Delta f_{\text{RF}}^\alpha}{\bar{\eta}_{\text{opt}}^\beta\Delta f_{\text{RF}}^\beta}\right)^2\frac{N_t^\beta}{N_t^\alpha}. \tag{11}$$

The imaging speed ratio SR indicates how much faster configuration α (with imaging speed s^α) is relative to configuration β (s^β). With the introduction of such SR, the optimal configuration as a function of the bandwidth or the focal plane sampling can easily be investigated qualitatively. One should note the cancellation of the NEP in (11).[8]

B. Focal Plane Sampling and Jiggling

The resolution of an imaging system $\Delta\theta$ is defined by its ability to distinguish between multiple sources. Suppose that two point sources are angularly displaced by $\Delta\theta$ in the far field of the quasi-optical system. The diffracted field arriving in the focal plane is a summation of two Airy discs,[9] which are transversely displaced in the focal plane by $\Delta\rho$ as is shown in Fig. 4(a). The geometrical relation between the angular displacement ($\Delta\theta$) of the point-sources and transverse displacement ($\Delta\rho$) of the Airy discs in the focal plane of an optical system with large $F_\#$ can be shown to be $\Delta\rho = F\Delta\theta$. The diffracted field is then sampled with a finite amount of antenna feeds in the focal plane. As is illustrated in Fig. 4(b), in order to be able to distinguish between the two incoherent sources in the focal plane image, one not only

[7] In the case that the system is cooled or any amplification circuitry is present, the background noise NEP_b [7], [31], [32] can become dominant. In such scenario, the NEP will also depend on source temperature, operational bandwidth, and optical efficiency. The NETD (9) will then reduce to an expression that is commonly found in microwave radiometer literature $\text{NETD} = \frac{T_S}{\sqrt{\Delta f_{\text{RF}}\tau_{\text{int}}}}$ [33], [34].

[8] Since we focus the study on uncooled power detectors, the NEP is considered to be independent on the signal received by the feeds.

[9] Airy disc $= C\frac{J_1(k\frac{\rho}{2F}D)}{k\frac{\rho}{2F}D}$ for broad-side illumination, where C is an intensity constant, k is the wavenumber, and ρ is the transversal focal plane position.

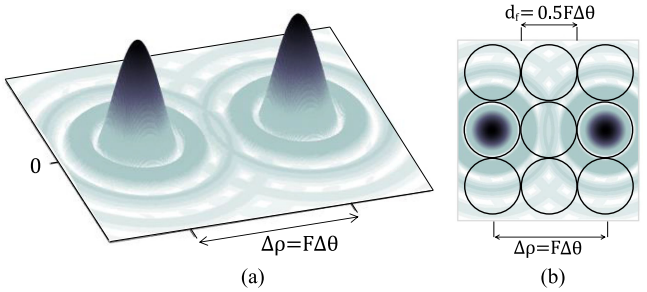

Fig. 4. (a) Diffracted field in the focal plane due to two point-sources separated by $\Delta\theta$. The focal plane image is a summation of two Airy discs which are separated by $\Delta\rho = F\Delta\theta$. (b) In order to resolve the sources in the focal plane, the feeds should be sampled with $d_f = 0.5F\Delta\theta$.

needs to sample the peaks of the Airy discs but also needs to sample in between in order to actually see a decrease in intensity and discriminate between the two peaks. The relation between an angular source separation $\Delta\theta$ and the required sampling d_f is then $d_f = \frac{\Delta\rho}{2} = 0.5F\Delta\theta$. By inverting this relationship, we can say that for a feed-size of d_f, the resolution of the imaging system is as follows:

$$\Delta\theta = 2\frac{d_f}{F}. \tag{12}$$

It is not possible to continue decreasing the feed-size d_f to achieve any resolution $\Delta\theta$ that is desired. The smallest resolution is indeed limited by the diffraction with the optics when the superposition of the two Airy discs only show one peak in the focal plane image. This minimal resolution $\Delta\theta^{\text{lim}}$ is approximately the -3 dB beamwidth of the diffracted intensity patterns [35]

$$\Delta\theta^{\text{lim}} \approx \frac{\lambda_c}{D} \tag{13}$$

where λ_c is the wavelength at the center frequency $f_c = \frac{f_{\min}+f_{\max}}{2}$ of the operational frequency band in which the antenna feeds are operating. Equating (13) with (12) gives rise to the sampling rule (14) stating that the diffraction-limited resolution $\Delta\theta^{\text{lim}}$ can be reached when the sampling points in the focal plane are separated by [35][10]

$$d_f^{\text{lim}} = 0.5F_{\#}\lambda_c. \tag{14}$$

When the antenna feeds are sampled according to (14), the FPA is referred to as *fully sampled*. Sparser sampling (i.e., *undersampling*) will result in a loss in resolution while denser sampling (i.e., *oversampling*) is never useful since the quasi-optical system's diameter limits the resolution. In this contribution, we will make use of undersampled arrays in order to maximize the imaging speed. The resolution will increase linearly with the undersampling factor N. The relationship between feed-size d_f and resolution $\Delta\theta$ can be written as

$$d_f = N \cdot 0.5F_{\#}\lambda_c \Longleftrightarrow \Delta\theta = N \cdot \Delta\theta^{\text{lim}}. \tag{15}$$

The resolution of an undersampled array ($N > 1$) is not diffraction limited, but as we will explain in the next section

[10]This sampling rule only applies when the signal is detected in intensity.

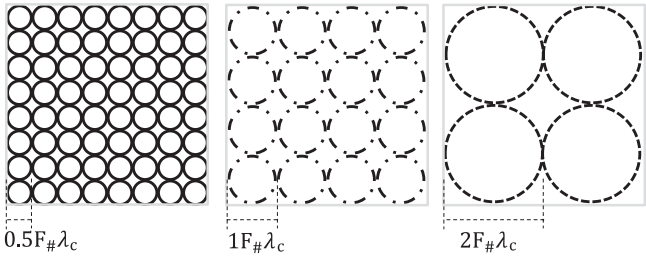

Fig. 5. Possible sampling configurations. Full sampling ($d_f = 0.5F_{\#}\lambda_c$), coherent sampling ($d_f = 1F_{\#}\lambda_c$), and maximum gain sampling ($d_f = 2F_{\#}\lambda_c$).

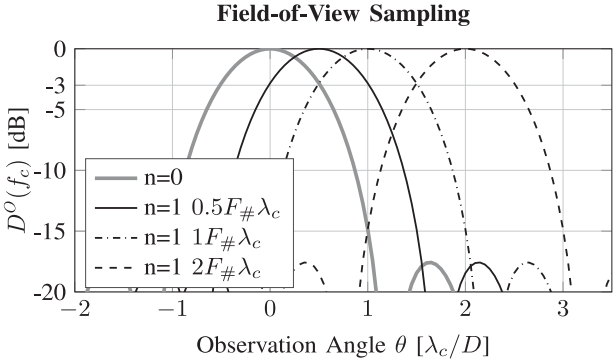

Fig. 6. Normalized patterns $D^O(f_c)$ after the optics of the on-axis ($n = 0$) and first adjacent feed (n=1) for all sampling configurations. Coherent sampling ($1F_{\#}\lambda_c$) and maximum gain sampling ($2F_{\#}\lambda_c$) requires jiggling in order to have a fully sampled FoV.

it is shown that the image quality does not only depend on the nominal resolution but also on the beam efficiency. A fully sampled FPA ($N = 1$) features the advantage that the image of the full FoV (with $\Delta\theta^{\text{lim}}$ resolution) is acquired without an integration time penalty [$N_t = 1$ in (10)] and with diffraction-limited optics. Unfortunately, the sampling requirement (14) leads to a low spill-over efficiency w.r.t. the quasi-optics ($\eta_{\text{so}}^{\Omega_O} \approx 0.15$) as shown in Fig. 3. This low efficiency will enter quadratically in the equation of the imaging speed (10). Luckily, the sampling rule (14) does not require the sampling points to be acquired simultaneously. Instead, one can decide to increase the size (and spacing) of individual feeds to $d_f = 1F_{\#}\lambda_c$ or $d_f = 2F_{\#}\lambda_c$ in order to increase the spill-over efficiency at the cost of the integration time. The sampling configurations $d_f = [0.5\ 1\ 2]F_{\#}\lambda_c$, as shown in Fig. 5, are respectively referred to as *fully-, coherent-, and maximum gain sampling*. For coherent- and maximum gain sampling, the spill-over efficiency will be increased to $\eta_{\text{so}}^{\Omega_O} \approx 0.46$ and $\eta_{\text{so}}^{\Omega_O} \approx 0.84$, respectively. The normalized patterns after the optics associated with two adjacent feeds are shown in Fig. 6 for the three different sampling configurations. The focal plane is undersampled for coherent- and maximum gain sampling. In order to obtain all the required sample points in a rectangular FPA, the optics have to be pointed in $N_t = 2 \times 2 = 4$ and $N_t = 4 \times 4 = 16$ directions, respectively, for coherently- and maximum gain sampled FPAs. This process of mechanical scanning is referred to as *jiggling*. For small FPAs, i.e., when $N_t = \frac{N_{\text{pix}}}{N_{\text{det}}} \gg 1$, the main limitation in achieving high imaging speeds is the implementation of the scanner [36]. However, as it is shown in [36, Table I], even for

TABLE I
IMAGING SPEED RATIO W.R.T. A FULLY SAMPLED ARRAY

d_f	$\bar{\eta}_{opt}$	N_t	SR
$0.5F_{\#}\lambda_c$	0.15	1	1
$1F_{\#}\lambda_c$	0.46	4	2.35
$2F_{\#}\lambda_c$	0.84	16	1.96

relatively small arrays ($<$ 100 elements), near real-time imaging speeds have been achieved. Therefore, with a maximum of only $N_t = 16$ scanning positions in this analysis, an additional time penalty associated with the mechanical scanner has been neglected.

III. FPA DESIGN

In this section, we will compare the imaging speed for different sampling configurations. Subsequently, the increase in imaging speed that one can obtain by exploiting a large operational frequency band is quantified. In the last section, it is illustrated that the imaging speed can further be improved by trading off in resolution.

A. FPA Configurations

The three different sampling configuration from Fig. 5 are compared relatively to each other using the imaging speed ratio defined in (11). The different FPAs are assumed to be operating with the same operational bandwidth Δf_{RF} and are sampled $d_f = [0.5\ 1\ 2]F_{\#}\lambda_c$ at the center frequency f_c. When including only the spill-over efficiency $\eta_{\mathrm{so}}^{\Omega_O}$ in the analysis ($\eta_{\mathrm{feed}} = 1$), the average optical efficiency can be approximated to be the spill-over efficiency at f_c, i.e., $\bar{\eta}_{\mathrm{opt}} \approx [0.15\ 0.46\ 0.84]$ for the sampling configurations $d_f = [0.5\ 1\ 2]F_{\#}\lambda_c$ respectively, as can be seen in Fig. 3. In the comparison of the different sampling configurations, we define the imaging speed ratio, $\mathrm{SR} = \frac{s^{\alpha}}{s^{\beta}}$, as the speed ratio of the coherent- and maximum gain sampled FPAs, $s^{\alpha} = s^{[1\ 2]F_{\#}\lambda_c}$, w.r.t. to the reference case of a fully sampled FPA, $s^{\beta} = s^{0.5F_{\#}\lambda_c}$. The imaging speed ratio approaches the limits as summarized in the fourth column of Table I.

It is beneficial to sample the feeds in the FPA coherently with $d_f = 1F_{\#}\lambda_c$ and to accept a small integration time penalty of $N_t = 4$ to sample the full FoV. A coherently sampled array is approximately 2.35 times faster w.r.t. the fully sampled FPA ($d_f = 0.5F_{\#}\lambda_c$). The fully sampled array is, in fact, the slowest focal plane architecture. The increase in spill-over efficiency for larger feed size is more significant than the introduced integration time penalty of $N_t = 4$.

B. Bandwidth Utilization

Most submillimeter-wave radiometric detectors are connected to integrated antennas that operate within a 20% fractional bandwidth [37]. A solution to make the detectors more sensitive is to increase the absolute bandwidth Δf_{RF} by using wideband antenna solutions [17], [25], [26], [38]. The imaging speed increases quadratically with the effective bandwidth

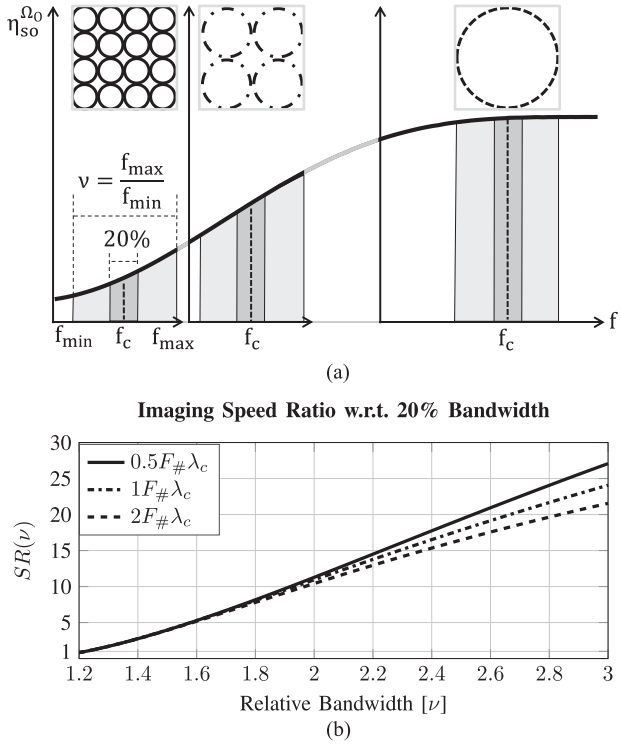

Fig. 7. The effect on imaging speed when using a large operational frequency band is studied w.r.t. the reference case of 20% fractional bandwidth. (a) The three sampling configurations, $d_f = 0.5F_{\#}\lambda_c$ (left), $d_f = 1F_{\#}\lambda_c$ (middle), and $d_f = 2F_{\#}\lambda_c$ (right) with $\nu = \frac{f_{\mathrm{max}}}{f_{\mathrm{min}}}$ relative bandwidth centered around f_c and with their associated reference cases of 20% fractional bandwidth. (b) Imaging speed ratio, $\mathrm{SR}(\nu) = \frac{s^{\alpha}(\nu)}{s^{\beta}(\nu=1.22)}$, as a function of the relative bandwidth w.r.t. the reference case.

$\bar{\eta}_{\mathrm{opt}}\Delta f_{\mathrm{RF}}$ (10). Let us investigate the improvement in imaging speed that one can obtain when a relative bandwidth ν, up to $\nu = \frac{f_{\mathrm{max}}}{f_{\mathrm{min}}} = 3$ centered around f_c, is used for each of the sampling configurations. The imaging speed ratio is defined as a function of this relative bandwidth ν

$$\mathrm{SR}(\nu) = \frac{s^{\alpha}(\nu)}{s^{\beta}(\nu = 1.22)}. \tag{16}$$

The reference case $s^{\beta}(\nu = 1.22)$ is defined with a 20% fractional bandwidth (20% fractional bandwidth is equivalent to a $\nu \approx 1.22$ relative bandwidth). This is illustrated in Fig. 7(a), where the three sampling configurations $d_f = [0.5\ 1\ 2]F_{\#}\lambda_c$ are sampled at f_c and have as reference case a 20% fractional bandwidth (dark gray area below the spill-over efficiency curve). For each configuration, the relative bandwidth ν is increased (light gray area below $\eta_{\mathrm{so}}^{\Omega_O}$) and is compared in speed to the reference case. This leads to the imaging speed ratios as are summarized in Fig. 7(b). For example, with a relative bandwidth of $\nu = 3$, the absolute bandwidth is increased by a factor of 5 w.r.t. the reference case, resulting in an increase in the imaging speed of approximately 25. Since the average spill-over efficiency does not change significantly as a function of the bandwidth (when sampled around f_c), there is not much difference between the imaging speed ratios of the three sampling configurations. Mainly due to this reason, it is important to note

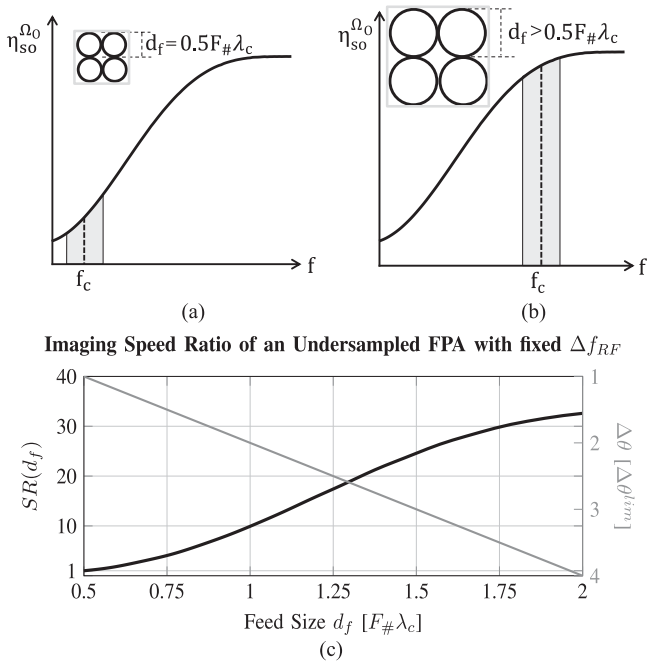

Fig. 8. The effect on imaging speed when using an undersampled array is studied w.r.t. a fully sampled array. The reference case, with imaging speed $s^{\beta}(d_f = 0.5F_{\#}\lambda_c)$, is shown in (a) and is a fully sampled FPA with $\Delta\theta^{\text{lim}} = \lambda_c/D$ resolution. The reference case is compared to $s^{\alpha}(d_f)$ as shown in (b), where the feed size is increased, leading to an undersampled array. In (c) the imaging speed ratio $\text{SR}(d_f) = \frac{s^{\alpha}(d_f)}{s^{\beta}(d_f = 0.5F_{\#}\lambda_c)}$ and resolution are shown as a function of the feed size d_f.

that also for wideband systems the coherent sampling configuration $d_f = 1F_{\#}\lambda_c$ is still the optimal FPA configuration. For the same absolute bandwidth, coherently sampling is faster with a factor of 2.35 w.r.t. the fully sampled FPA, as we concluded in the previous section (see Table I).

C. Maximizing Imaging Speed With an Undersampled FPA

In the case that the detectors are not sufficiently sensitive at the desired imaging speed, two practical solutions exist to improve the sensitivity or imaging speed at the cost of (potential) resolution: by increasing the feed size d_f (until $2F_{\#}\lambda_c$) or by translating the frequency band of operation to a higher portion in the spectrum (assuming the NEP is not affected). As explained in Section II-B, without performing any jiggling, the FPA becomes undersampled for $d_f > 0.5F_{\#}\lambda_c$, such that the optics do not offer a diffraction limited resolution (15).

In the first solution, the feed size d_f is increased. Let us define the imaging speed ratio as a function of the feed size

$$\text{SR}(d_f) = \frac{s^{\alpha}(d_f)}{s^{\beta}(d_f = 0.5F_{\#}\lambda_c)}. \tag{17}$$

The reference case, with imaging speed $s^{\beta}(d_f = 0.5F_{\#}\lambda_c)$, is a fully sampled FPA as is illustrated in Fig. 8(a). The feed size is increased while the bandwidth is kept fixed with a 20% fractional bandwidth centered around f_c. A larger feed size results in an increase in spill-over efficiency and therefore imaging speed $s^{\alpha}(d_f)$, as illustrated in Fig. 8(b) and quantified in Fig. 3. The imaging speed ratio $\text{SR}(d_f)$ is shown in Fig. 8(c) with the black curve and left y-axis. For the same absolute bandwidth and without jiggling, the imaging speed ratio is increasing quadratically with the spill-over efficiency. When the feed size is $d_f = 2F_{\#}\lambda_c$, the FPA is faster with a factor of 32. This increase in imaging speed comes at the cost of resolution. Referring back to (15), for a feed size of $d_f = 2F_{\#}\lambda_c$, the resolution is not diffraction limited: $\Delta\theta = 4\Delta\theta^{\text{lim}}$ since the pointing direction of the patterns associated with two adjacent feeds ($n = 0$ and $n = 1$ $d_f = 2F_{\#}\lambda_c$ in Fig. 6) is increased. The resolution, as a function of the feed size, is shown by the gray curve and the right axis in Fig. 8(c). Of course, one could compensate for this decrease in resolution by increasing the size of the optics.

The second option, if the technology and application allows for it, is to translate the frequency band of operation to a higher portion in the spectrum. This higher frequency band is defined with a new center frequency f_c'. Although the physical feed size remains unchanged, the electrical size (in terms of λ_c') grows linearly with f_c'/f_c, which contributes to the same increase in imaging speed as shown in Fig. 8(c). Furthermore, an additional increase of $(f_c'/f_c)^2$ in imaging speed can be expected since the absolute bandwidth increases with a factor f_c'/f_c when the fractional bandwidth is kept fixed.

For example, if one initially operates with a fully sampled FPA $d_f = 0.5F_{\#}\lambda_c$ around f_c but decides to increase in imaging speed by translating the frequency band to $f_c' = 4f_c$ (i.e., maximum gain sampling $d_f = 2F_{\#}\lambda_c'$ with the same physical feed size) one expects a factor of $32 \times 16 = 512$ increase in imaging speed, where the factor 32 is the result of the increase in spill-over efficiency and the factor $(\frac{f_c'}{f_c})^2 = 16$ is the result of the increase in absolute bandwidth.

In the following section, we will see that in an imaging scenario an undersampled array is actually beneficial in terms of image quality.

IV. Image Quality in Undersampled Arrays

In the previous section, it was explained that a significant increase in imaging speed can be achieved when operating in a higher frequency band with center frequency $f_c' > f_c$. When the physical feed size is not altered, the resolution is not changed, although it is not anymore diffraction limited (15). In this section, we will see that in an imaging scenario the image quality of an undersampled array does improve w.r.t. a fully sampled array with the same resolution. For this study, we introduce a beam efficiency of the effective gain patterns [$G_{\text{eff}}(\Omega)$ defined in (7b)]. The beam efficiency is, in essence, the spill-over efficiency of a pixel w.r.t. the angular region associated with that specific pixel. This angular region we refer to as the *pixel region* (referring to the centered feed $n = 0$ in Fig. 6, its associated pixel region subtends $\phi \in (0, 2\pi), \theta \in (0, \frac{\lambda_c}{4D})$).

Let us consider a fully sampled array as is illustrated in the left-hand side of Fig. 9(a). We consider both a narrowband ($\nu = 1.22$) and wideband ($\nu = 3$) FPA. The normalized effective gain patterns of three adjacent feeds in the FPA are shown on the left-hand side of Fig. 9(b). The beam patterns of adjacent feeds have a significant overlap. This means that a pixel shares a

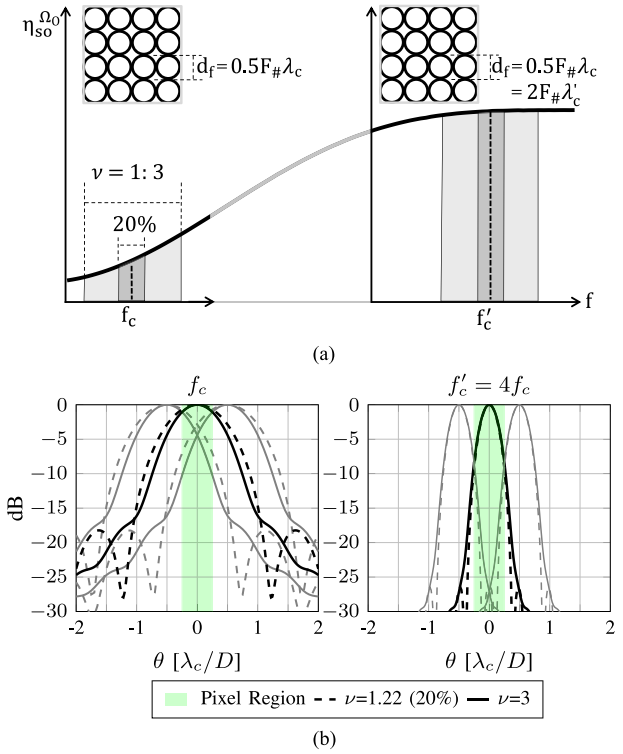

Fig. 9. (a) FPAs under investigation for calculating the effective gain patterns. For both FPAs a $\nu = 1.22$ and a $\nu = 3$ relative bandwidth are investigated. (b) Normalized effective gain patterns $G_{\text{eff}}(\Omega)$ (7b) for three adjacent feeds of the FPAs depicted in (a). The angular pixel region associated with the on-axis pixel is highlighted.

significant portion of incident power with adjacent pixels, the pixels are not well restricted to their own pixel region. This pixel region is also indicated in Fig. 9(b) by the green bar.

Consider now the same FPA but operating in a frequency band around $f_c' = 4f_c$, as illustrated in the right-hand side of Fig. 9(a). The normalized effective gain patterns of adjacent feeds are shown on the right-hand side of Fig. 9(b). Since the feed size remains the same, the pointing direction of the beam patterns is also unchanged. Both FPA configurations have therefore the same resolution. However, the FPA operating around $f_c' = 4f_c$ operates in a higher frequency band, such that the beam patterns become more directive. The pixels are significantly better isolated in their pixel region.

Let us quantify this pixel isolation by introducing a beam efficiency, BE, that describes how well the effective gain pattern is isolated from the patterns associated with adjacent pixel regions. The beam efficiency can be defined by angularly integrating the beam pattern over the pixel region that is associated with that particular feed, which for the on-axis feed results in the following equation:

$$\text{BE} = \frac{\int_0^{2\pi} \int_0^{\frac{\lambda_c}{4D}} G_{\text{eff}}(\theta) \sin\theta d\theta d\phi}{\int_0^{2\pi} \int_0^{\pi/2} G_{\text{eff}}(\theta) \sin\theta d\theta d\phi}. \tag{18}$$

The beam efficiency is shown in Fig. 10 as a function of the translated center frequency f_c'. If the array is fully sampled for the frequency band of operation ($f_c' = f_c$), the beam patterns

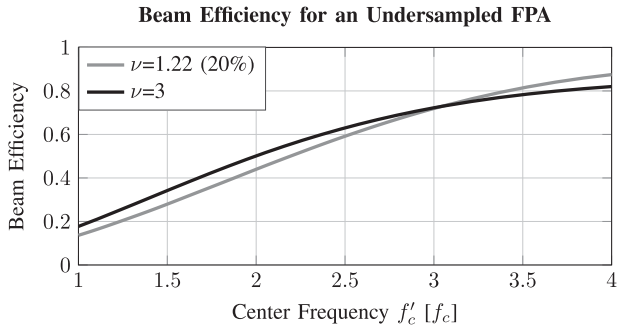

Fig. 10. Beam efficiency as calculated with (18). The beam efficiency describes how well the effective gain pattern is coupled to the angular region subtended by the pixel ($\phi \in (0, 2\pi), \theta \in (0, \frac{\lambda_c}{4D})$ for the centered feed).

are not well restricted to their own pixel region, with a BE $\approx 15\%$ the feed will mainly integrate power from adjacent pixel regions. Instead, by undersampling the FPA to $f_c' = 4f_c$, the beam patterns will be more directive and the beam efficiency is higher than 80%, i.e., the beam patterns are well isolated from adjacent feeds. No significant difference in BE between narrowband and wideband systems can be observed.

The beam efficiency does impact the temperature sensitivity of the system. Despite the fact that the analysis is derived for distributed sources, it should be noted that a high BE implies that the system is less sensitive to isolated sources at the edges of a pixel region. Instead, for distributed sources, a high BE improves the sensitivity since the BE can, in fact, be included as an additional spill-over term in the evaluation of P_a^n (5), while simultaneously considering the power arriving from adjacent pixels to be contributing to the noise power.

Consider the following imaging example to investigate the effect of the beam efficiency on the quality of image reconstruction. The THz-sensing-group logo is defined with a source temperature $T_S(\Omega)$ and is angularly distributed in space. The logo is projected in the u, v-domain ($u = \sin(\theta)\cos(\phi)$ and $v = \sin(\theta)\sin(\phi)$) in Fig. 11(a). The solid angle subtended by the source distribution is assumed so small, such that $\sin\theta \approx \theta$ and the projection in the u, v domain can be normalized to the angular pixel dimension, $\lambda_c/2D$. The temperature distribution $T_S(\Omega)$ is defined from 0 to 255 K, as is shown by the color bar. Indicated by the box is the FoV under investigation, which corresponds to the FoV of 100×100 elements in a fully sampled FPA. A zoom-in on the letter *S* is shown, illustrating the pixel regions of 6×6 elements in the FPA. The received power by the nth feed P_a^n can be calculated by using (7a). Subsequently, by using the approximation on average received power $\bar{P}_a$ (8a), the temperature distribution of the source can be reconstructed to be the following equation:

$$T_S^{\text{rec}}(\Omega_n) = \frac{P_a^n}{k_B \bar{\eta}_{\text{opt}} \Delta f_{\text{RF}}} = \frac{\int_{\Omega_S} T_S(\Omega) G_{\text{eff}}(\Omega - \Omega_n) d\Omega}{4\pi \bar{\eta}_{\text{opt}} \Delta f_{\text{RF}}}. \tag{19}$$

The reconstructed thermal image of the source distribution T_S^{rec} is shown in the top two figures of Fig. 11(b) for the fully sampled FPA ($f_c' = f_c$) with its associated effective gain pattern in the left subfigure in Fig. 9(b). By repeating the procedure

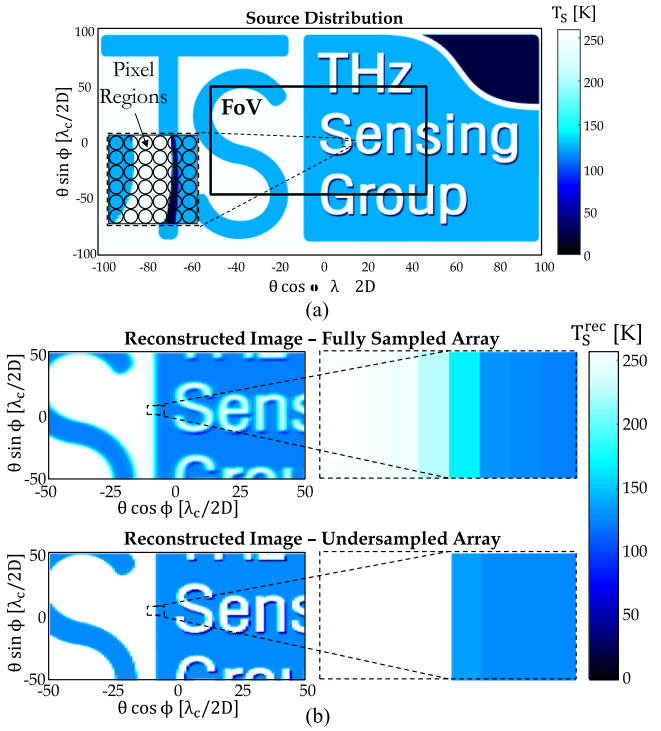

Fig. 11. THz-sensing Group logo as source distribution in (a) and the reconstructed images in (b) for a fully sampled and undersampled array. (a) Source distribution projected in the u, v-domain using $u = \theta\cos(\phi)$ and $v = \theta\sin(\phi)$. Indicated is the FoV of a 100×100 element FPA and a zoom-in on the letter *S* showing the pixel regions of 6×6 elements. The color bar on the right shows the temperature distribution T_s of the logo. (b) Reconstructed image of the source distribution shown in Fig. 11(a) in the case that the image is acquired using a fully sampled FPA and an undersampled FPA with $f_c' = 4f_c$. The reconstructed image is calculated by using (19). A zoom-in of the transitions between the white and blue regions are shown.

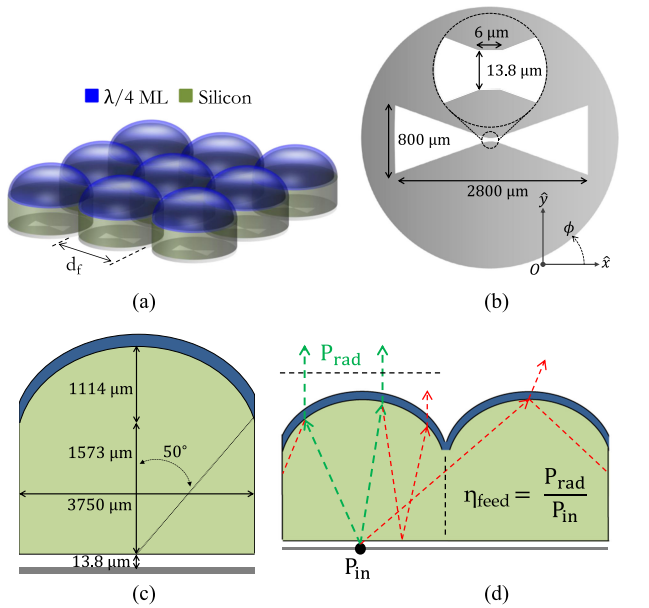

Fig. 12. Leaky lens antennas [26] serving as reflector feeds in FPA as depicted in (a). The dimensions of the slot and elliptical lenses are shown in (b) and (c) respectively. The definition of feed efficiency is illustrated in (d).

with the effective gain pattern [right subfigure in Fig. 9(b)] of the undersampled array ($f_c' = 4f_c$), one obtains the bottom two reconstructed images in Fig. 11(b). When both reconstructed images are compared, we can see that the letters Sens and the transition from white to blue are significantly sharper for the undersampled array due to a higher beam efficiency. Whereas the feeds in a fully sampled array, with a BE $\approx 15\%$, receives power from several pixel regions away, the undersampled array is better isolated with BE $\approx 80\%$, which results in an improved image reconstruction.

For this reason, the image quality can be qualified both in terms of the nominal resolution $\Delta\theta$ due to the angular discretization of the beams and in terms of the beam efficiency.

V. Realistic Feeds

In the previous analysis, we made use of uniformly illuminated and ideal feeds. In this section, we will instead show the performance of a realistic antenna design. The modeling techniques that are used in this section are the same that have been used in the last years by some of the authors for the development and characterization of lens antenna FPAs for passive astronomical instruments. The predicted performance of the lens antennas show excellent agreement with measurements [3], [39].

In order to appreciate the applicability of this study, we will consider an FPA containing wideband leaky lens antenna feeds as is shown in Fig. 12(a) [26]. The radiation performance of a single leaky lens has been measured at low frequency in [40] and at high frequency in [41] and [42]. After introducing the quasi-optical system containing leaky lens feeds, a comparison in terms of imaging speed will be made with narrowband conical horn-antenna feeds.

The leaky lens feeds operate from 200 to 600 GHz ($\nu = 3$) and illuminate a parabolic reflector with $F_\# = 2.5$. In order to optimize the imaging speed, we place the feeds in a maximum gain sampled array ($d_f = 2F_\#\lambda_c$) at $f_c = 400$ GHz *without* mechanically jiggling the FPA. Note that this FPA is equivalent to the scenario discussed in Fig. 8 with $d_f = 2F_\#\lambda_c$; the array is undersampled to maximize the imaging speed. The resolution is not diffraction limited with $\Delta\theta = 4\Delta\theta^{\text{lim}} = 4\frac{\lambda_c}{D}$. The feeds are optimized and analyzed by numerical CST simulations [43], leading to the dimensions of the slot and elliptical lens as are shown in Fig. 12(b) and (c), respectively. The dimensioning of the elliptical lens is corrected for a phase center of 126 μm behind the slot and the 50° truncation is at approximately the -10 dB beamwidth of the fields inside the lens at 200 GHz. In Fig. 13, the patterns of the leaky lens antennas are plotted for $f = 250$ and 550 GHz. As a reference, the patterns indicated with *uniform* are associated with uniformly illuminated feeds with the same feed size d_f, as those used throughout the previous sections. The pattern region that is subtended by the reflector is indicated by θ_0. The reflector patterns are obtained by physical-optics in GRASP [44].

The feed efficiency η_{feed}, the spill-over efficiency w.r.t. the reflector $\eta_{\text{so}}^{\Omega_O}$, and the optical efficiency $\eta_{\text{opt}} = \eta_{\text{feed}}\eta_{\text{so}}^{\Omega_O}$ are shown in Fig. 14 by the solid lines. It is important to note that the feed efficiency is defined as the ratio of the power

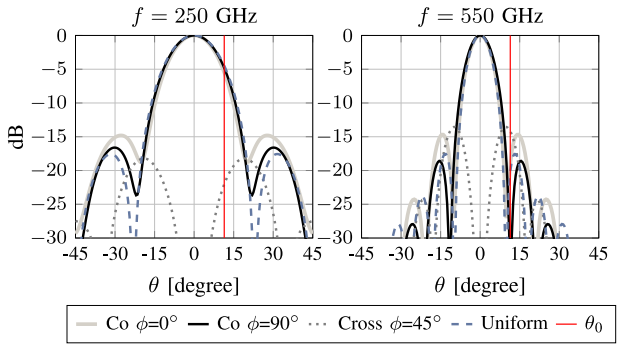

Fig. 13. Feed patterns of the leaky lens antennas compared to the pattern of a uniformly illuminated feed with the same diameter. Indicated with θ_0 is the angle subtended by a reflector for a $F_{\#} = 2.5$ configuration.

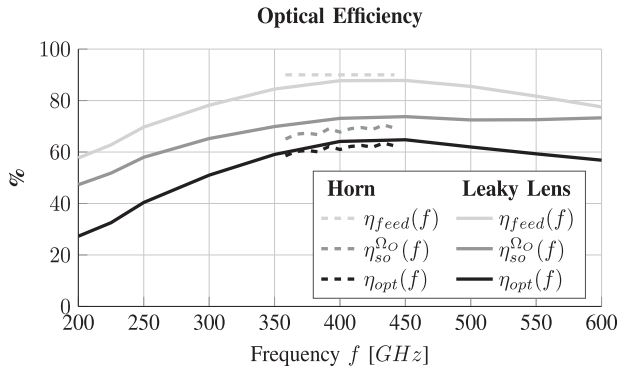

Fig. 14. Optical efficiency for both the leaky lens (solid) FPA and horn (dashed) FPA.

radiated by the leaky lens P_{rad}, and the power presented to the port P_{in}, where any radiated power that is first reflected inside the lens or substrate is omitted. This is visualized in Fig. 12, where only the green, reflection free, rays contribute to the radiated power P_{rad}. Power leaving the leaky lens after the first reflection is not expected to be captured by the reflector. The average optical efficiency of the reflector system illuminated by the leaky lenses is $\bar{\eta}_{\mathrm{opt}} = 55.3\%$, leading to an effective bandwidth of $\Delta f_{\mathrm{RF}}^{\mathrm{eff}} = 0.553 \cdot 400\ \mathrm{GHz} = 221\ \mathrm{GHz}$.

A significant advantage of the described leaky lens structure is that it is fully integrated. This means that it can be used in large FPAs. Furthermore, impedance matching over the full operational bandwidth is simple to achieve. Instead, feeding- and matching-architectures for a large integrated FPA based on horn antennas is proven to be a difficult task [45] when fractional bandwidths larger than 20% are desired. Let us compare the leaky lens FPA with an FPA containing conical horn antennas, sampled identically to the leaky lens antennas with $d_f = 2F_{\#}\lambda_c$. The horn antennas are operating in a 20% fractional bandwidth from 360 to 440 GHz, as indicated in Fig. 14. Their efficiencies are shown by the dashed lines. The horn antennas are simulated without any losses or feeding network. Instead, we define the feed efficiency optimistically at 90% over the full band. The average optical efficiency is 61.5% leading to an effective bandwidth of $\Delta f_{\mathrm{RF}}^{\mathrm{eff}} = 49.2$ GHz. The imaging speed ratio (11) of the leaky lens-based FPA w.r.t. the horn-antenna-based FPA is $\mathrm{SR} = \frac{s^{\text{Leaky-Lens}}}{s^{\text{Horn}}} = (\frac{221}{49.2})^2 = 20$. This SR is indeed close to the predicted value in Fig. 7 of $\mathrm{SR}(\nu = 3) = 21.5$.

Referring back to Fig. 1, an effective bandwidth of 221 GHz is sufficient to achieve a 1 K sensitivity and a 10 Hz refresh rate imaging requirement, provided that the detectors have an NEP of 1.4 $\mathrm{pW}/\sqrt{\mathrm{Hz}}$. Recently conducted measurements [46] of a *dual polarized* leaky lens antenna show that the received power (5) from an incoherent source is increased by a factor of 2 compared to a single polarized version of the antenna. In that scenario, the requirement on the detector NEP is relaxed by the same factor. This demonstrates that a practical sensitivity and imaging speed can be achieved with an uncooled and fully passive integrated FPA. The horn-antenna-based FPA on the other hand, with an effective bandwidth of 49.2 GHz, will require cooling or amplification circuitry to achieve the practical imaging requirements.

VI. Conclusion

Uncooled submillimeter-wave direct detectors are characterized by moderate sensitivities due to high electronic noise and thus are not often proposed for real-time imaging. In this contribution, the design guidelines for focal plane architectures based on antenna-coupled direct detectors are proposed with greatly enhanced potential speeds, thanks to the efficient use of the available spectral bandwidth at submillimeter wavelengths. Relying on the guidelines and focal plane architectures introduced in this paper, it is shown that real-time imaging with high sensitivities can be achieved with already available practical detectors.

References

[1] G. Chattopadhyay, "Technology, capabilities, and performance of low power terahertz sources," *IEEE Trans. THz Sci. Technol.*, vol. 1, no. 1, pp. 33–53, Sep. 2011.
[2] R. A. Hadi *et al.*, "A 1 k-pixel video camera for 0.7–1.1 terahertz imaging applications in 65-nm CMOS," *IEEE J. Solid-State Circuits*, vol. 47, no. 12, pp. 2999–3012, Dec. 2012.
[3] J. J. A. Baselmans *et al.*, "A kilo-pixel imaging system for future space based far-infrared observatories using microwave kinetic inductance detectors," *Astron. Astrphys.*, vol. 601, May 2017, Art. no. A89.
[4] S. Rowe *et al.*, "A passive terahertz video camera based on lumped element kinetic inductance detectors," *Rev. Sci. Instrum.*, vol. 87, no. 3, Mar. 2016, Art. no. 033105.
[5] T. G. Blaney, "Radiation detection at submillimetre wavelengths," *J. Phys. E, Sci. Instrum.*, vol. 11, no. 9, pp. 856–881, Sep. 1978.
[6] R. Appleby and H. B. Wallace, "Standoff detection of weapons and contraband in the 100 GHz to 1 THz region," *IEEE Trans. Antennas Propag.*, vol. 55, no. 11, pp. 2944–2956, Nov. 2007.
[7] P. L. Richards, "Bolometers for infrared and millimeter waves," *J. Appl. Phys.*, vol. 76, no. 1, pp. 1–24, Jul. 1994.
[8] T. May *et al.*, "Safe VISITOR: Visible, infrared, and terahertz object recognition for security screening application," in *Proc. SPIE*, vol. 7309, May 2009, Art. no. 73090E.
[9] A. Timofeev *et al.*, "Optical and electrical characterization of a large kinetic inductance bolometer focal plane array," *IEEE THz Sci. Technol.*, vol. 7, no. 2, pp. 218–224, Mar. 2017.
[10] E. Grossman *et al.*, "Passive terahertz camera for standoff security screening," *Appl. Opt.*, vol. 49, no. 19, pp. E106–E120, Jul. 2010.
[11] M. J. Griffin, J. J. Bock, and W. K. Gear, "Relative performance of filled and feedhorn-coupled focal-plane architectures," *Appl. Opt.*, vol. 41, no. 31, pp. 6543–6554, Nov. 2002.
[12] E. R. Brown and D. Segovia-Vargas, "Principles of THz direct detection," in *Semiconductor Terahertz Technology: Devices and Systems at Room Temperature Operation*, G. Carpintero, L. E. García Muñoz,H. L. Hartnagel, S. Preu, and A. V. Räisänen, Eds. Chichester, U.K.: Wiley, Jul. 2015, pp. 212–253.

[13] D. Y. Kim, S. Park, R. Han, and K. K. O, "Design and demonstration of 820-GHz array using diode-connected NMOS transistors in 130-nm CMOS for active imaging," *IEEE THz Sci. Technol.*, vol. 6, no. 2, pp.306–317, Mar. 2016.
[14] R. Han *et al.*, "Active terahertz imaging using Schottky diodes in CMOS: Array and 860-GHz pixel," *IEEE J. Solid-State Circuits*, vol. 48, no. 10, pp. 2296–2308, Oct. 2013.
[15] F. Schuster *et al.*, "A broadband THz imager in a low-cost CMOS technology," in *Proc. IEEE Int. Solid-State Circuits Conf.*, Feb. 2011, pp. 42–43.
[16] N. Oda *et al.*, "Microbolometer terahertz focal plane array and camera with improved sensitivity in the sub-terahertz region," *J. Infrared, Millimeter, THz Waves*, vol. 36, no. 10, pp. 947–960, Oct. 2015.
[17] G. C. Trichopoulos, H. L. Mosbacker, D. Burdette, and K. Sertel, "A broadband focal plane array camera for real-time THz imaging applications," *IEEE Trans. Antennas Propag.*, vol. 61, no. 4, pp. 1733–1740, Apr. 2013.
[18] D. Dufour *et al.*, "Review of terahertz technology development at INO," *J. Infrared, Millimeter, THz Waves*, vol. 36, no. 10, pp. 922–946, Oct. 2015.
[19] J. Oden *et al.*, "Imaging of broadband terahertz beams using an array of antenna-coupled microbolometers operating at room temperature," *Opt. Express*, vol. 21, no. 4, pp. 4817–4825, Feb. 2013.
[20] C. Dietlein, A. Luukanen, F. Meyer, Z. Popovic, and E. Grossman, "Phenomenology of passive broadband terahertz images," in *Proc. 4th ESA Workshop Millimetre-Wave Technol. Appl.*, Feb. 2006, pp. 405–410.
[21] G. Rieke, *Detection of Light: From the Ultraviolet to the Submillimeter*. Cambridge, U.K.: Cambridge Univ. Press, 2003.
[22] R. Han *et al.*, "A 280-GHz Schottky diode detector in 130-nm digital CMOS," *IEEE J. Solid-State Circuits*, vol. 46, no. 11, pp. 2602–2612, Nov. 2011.
[23] Virginia Diodes, Inc., 2017. [Online]. Available: http://vadiodes.com/index.php/en/products/detectors#zero-bias-detector, Accessed on: Jul. 18, 2017.
[24] Y. Kurita *et al.*, "Ultrahigh sensitive sub-terahertz detection by inp-based asymmetric dual-grating-gate high-electron-mobility transistors and their broadband characteristics," *Appl. Phys. Lett.*, vol. 104, no. 25, Jun. 2014, Art. no. 251114.
[25] O. Yurduseven, D. Cavallo, A. Neto, G. Carluccio, and M. Albani, "Parametric analysis of extended hemispherical dielectric lenses fed by a broadband connected array of leaky-wave slots," *IET Microw., Antennas Propag.*, vol. 9, no. 7, pp. 611–617, May 2015.
[26] O. Yurduseven, N. Llombart, and A. Neto, "A dual-polarized leaky lens antenna for wideband focal plane arrays," *IEEE Trans. Antennas Propag.*, vol. 64, no. 8, pp. 3330–3337, Aug. 2016.
[27] S. van Berkel, E. Malotaux, D. Cavallo, M. Spirito, A. Neto, and N. Llombart, "Wideband single pixel radiometer in CMOS," in *Proc. 42nd Int. Conf. Infrared, Millimeter THz Waves*, 2017.
[28] S. Malz, R. Jain, and U. R. Pfeiffer, "Towards passive imaging with CMOS THz cameras," in *Proc. 41st Int. Conf. Infrared, Millimeter, THz Waves*, 2016, pp. 1–2.
[29] M. Planck, *The Theory of Heat Radiation*, vol. 6. North Chelmsford, MA, USA: Courier Corp., 1914, p. 1023.
[30] A. Luukanen, R. Appleby, M. Kemp, and N. Salmon, "Millimeter-wave and terahertz imaging in security applications," in *Terahertz Spectroscopy and Imaging* (Optical Sciences), vol 171, K. E. Peiponen, A. Zeitler, and M. Kuwata-Gonokami, Eds. New York, NY, USA: Springer, 2012, pp. 491–520.
[31] R. W. Boyd, "Photon bunching and the photon-noise-limited performance of infrared detectors," *Infrared Phys.*, vol. 22, no. 3, pp. 157–162, May 1982.
[32] D. Flanigan *et al.*, "Photon noise from chaotic and coherent millimeter-wave sources measured with horn-coupled, aluminum lumped-element kinetic inductance detectors," *Appl. Phys. Lett.*, vol. 108, no. 8, Feb. 2016, Art. no. 083504.
[33] M. Tiuri, "Radio astronomy receivers," *IEEE Trans. Antennas Propag.*, vol. 12, no. 7, pp. 930–938, Dec. 1964.
[34] J. W. May, "SiGe integrated circuits for millimeter-wave imaging and phased arrays," Ph.D. dissertation, 2009. [Online]. Available: http://www.escholarship.org/uc/item/5488f0g9
[35] J. F. Johansson, "Millimeter-wave imaging theory and experiments," Onsala Space Observatory, Onsala, Sweden, Res. Rep. no. 151, 1986.
[36] E. Gandini, J. Svedin, T. Bryllert, and N. Llombart, "Optomechanical system design for dual-mode stand-off submillimeter wavelength imagers," *IEEE THz Sci. Technol.*, vol. 7, no. 4, pp. 393–403, Jul. 2017.
[37] D. F. Filipovic, S. S. Gearhart, and G. M. Rebeiz, "Double-slot antennas on extended hemispherical and elliptical silicon dielectric lenses," *IEEE Trans. Microw. Theory Techn.*, vol. 41, no. 10, pp. 1738–1749, Oct. 1993.
[38] A. J. Alazemi, H. H. Yang, and G. M. Rebeiz, "Double bow-tie slot antennas for wideband millimeter-wave and terahertz applications," *IEEE THz Sci. Technol.*, vol. 6, no. 5, pp. 682–689, Aug. 2016.
[39] L. Ferrari *et al.*, "Antenna coupled MKID performance verification for large format astrophysics arrays," *IEEE THz Sci. Technol.*, to be published.
[40] A. Neto, S. Monni, and F. Nennie, "UWB, non dispersive radiation from the planarly fed leaky lens antenna—Part II: Demonstrators and measurements," *IEEE Trans. Antennas Propag.*, vol. 58, no. 7, pp. 2248–2258, Jul. 2010.
[41] A. Neto, N. Llombart, J. J. A. Baselmans, A. Baryshev, and S. J. C. Yates, "Demonstration of the leaky lens antenna at submillimeter wavelengths," *IEEE THz Sci. Technol.*, vol. 4, no. 1, pp. 26–32, Jan. 2014.
[42] J. Bueno *et al.*, "Full characterisation of a background limited antenna coupled KID over an octave of bandwidth for THz radiation," *Appl. Phys. Lett.*, vol. 110, no. 23, Jun. 2017, Art. no. 233503.
[43] *CST Microwave StudioVersion 2014.00*, Comput. Simul. Technol. AG, Darmstadt, Germany, 2014.
[44] *GRASP Version 10.5.0*, TICRA, Copenhagen, Denmark, 2015.
[45] J. W. Kooi *et al.*, "A full-height waveguide to thin-film microstrip transition with exceptional RF bandwidth and coupling efficiency," *Int. J. Infrared Millimeter Waves*, vol. 24, no. 3, pp. 261–284, Sep. 2003.
[46] J. Bueno, O. Yurduseven, N. Llombart, S. Yates, A. Neto, and J. Baselmans, "Experimental validation of an mkid coupled dual polarized leaky lens antenna," in *Proc. 42nd Int. Conf. Infrared, Millimeter THz Waves*, 2017.

Sven van Berkel (S'16) received the B.Sc. and M.Sc. degrees (*cum laude*) in electrical engineering from the Delft University of Technology (TU Delft), Delft, The Netherlands, in 2012 and 2015, respectively. He is currently working toward the Ph.D. degree at the Terahertz Sensing Group, TU Delft. During his Master's, he specialized in telecommunications engineering with a focus on antennas and electromagnetic wave theory.

His research interests include passive imaging systems, ultra-wideband antennas for millimeter and submillimeter-wave applications, and quasi-optical systems and analytical/numerical techniques in electromagnetics and transmission line characterization.

Ozan Yurduseven (S'11) received the B.Sc. and M.Sc. (Hons.) degrees in electronics and communications engineering from Yildiz Technical University, Istanbul, Turkey, in 2009 and 2011, respectively, and the Ph.D. degree in electrical engineering from the Delft University of Technology, Delft, The Netherlands, in 2016. His Ph.D. research concerned the development of dielectric lens antennas for THz space applications.

During his Ph.D., he spent six months as a Visiting Researcher with the Instituto de Telecomunicações, Instituto Superior Técnico, Lisbon, Portugal, where he was involved with double shell dielectric lenses. He has authored or co-authored more than 30 publications in peer-reviewed journals and conferences. His current research interests include dielectric lens antennas for millimeter and submillimeter-wave space applications, quasi-optical systems, numerical techniques in electromagnetics, and metamaterials.

Dr. Yurduseven is a member of the IEEE Antennas and Propagation Society and the European Association on Antennas and Propagation. He was the recipient of the Best Student Paper Award of the European Conference on Antennas and Propagation (EuCAP) in 2013. He was a co-recipient of the Best Paper on Electromagnetism and Antenna Theory of EuCAP 2016. He serves as a Reviewer for the IEEE TRANSACTIONS ON ANTENNAS AND PROPAGATION, IEEE ANTENNAS AND WIRELESS PROPAGATION LETTERS and *IET Microwaves, Antennas and Propagation*.

Angelo Freni (S'90–M'91–SM'03) received the Laurea (Doctors) degree in electronics engineering from the University of Florence, Florence, Italy, in 1987.

Since 1990, he has been with the Department of Electronic Engineering, University of Florence, first as an Assistant Professor and, since 2002, as an Associate Professor of electromagnetism. From 1995 to 1999, he has also been an Adjunct Professor with the University of Pisa, Pisa, Italy, and since 2010, a Visiting Professor with the TU Delft University of Technology, Delft, The Netherlands. During 1994, he was involved in research with the Engineering Department, University of Cambridge, Cambridge, U.K., concerning the extension and the application of the finite element method to the electromagnetic scattering from periodic structures. From 2009 to 2010, he also spent one year as a Researcher with the TNO Defence, Security and Safety, The Hague, The Netherlands, where he was involved with the electromagnetic modeling of kinetic inductance devices and their coupling with array of slots in the THz range. His research interests include meteorological radar systems, radiowave propagation, numerical and asymptotic methods in electromagnetic scattering and antenna problems, electromagnetic interaction with moving media, and remote sensing. In particular, part of his research concerned numerical techniques based on the integral equation with a focus on domain-decomposition and fast solution methods.

Andrea Neto (M'00–SM'10–F'16) received the Laurea degree (*summa cum laude*) in electronic engineering from the University of Florence, Florence, Italy, in 1994, and the Ph.D. degree in electromagnetics from the University of Siena, Siena, Italy, in 2000. Part of his Ph.D. degree was developed at the European Space Agency Research and Technology Center Noordwijk, The Netherlands.

He worked for the Antenna Section at the European Space Agency Research and Technology Center for over two years. From 2000 to 2001, he was a Postdoctoral Researcher with the California Institute of Technology, Pasadena, CA, USA, where he worked with the Sub-mm Wave Advanced Technology Group. From 2002 to January 2010, he was a Senior Antenna Scientist with TNO Defence, Security, and Safety, The Hague, The Netherlands. In February 2010, he became a Full Professor of applied electromagnetism with the EEMCS Department, Technical University of Delft, Delft, The Netherlands, where he formed and leads the THz Sensing Group. His research interests include the analysis and design of antennas with an emphasis on arrays, dielectric lens antennas, wideband antennas, EBG structures, and THz antennas.

Dr. Neto served as an Associate Editor of the IEEE TRANSACTIONS ON ANTENNAS AND PROPAGATION (2008–2013) and IEEE ANTENNAS AND WIRELESS PROPAGATION LETTERS (2005–2013). He is a member of the Technical Board of the European School of Antennas and organizer of the course on antenna imaging techniques. He is a member of the Steering Committee of the Network of Excellence NEWFOCUS, dedicated to focusing techniques in mm and sub-mm wave regimes. In 2011, he was the recipient of the European Research Council Starting Grant to perform research on Advanced Antenna Architectures for THz Sensing Systems. He was the recipient of the H. A. Wheeler Award for the best applications paper of 2008 in the IEEE TRANSACTIONS ON ANTENNAS AND PROPAGATION, the Best Innovative Paper Prize of the 30th ESA Antenna Workshop in 2008, and the Best Antenna Theory Paper Prize of the European Conference on Antennas and Propagation (EuCAP) in 2010. In 2011, he was the recipient of the European Research Council Starting Grant to perform research on advanced antenna architectures for THz sensing systems.

Nuria Llombart (S'06–M'07–SM'13) received the Master's degree in electrical engineering and Ph.D. degree from the Polytechnic University of Valencia, Valencia, Spain, in 2002 and 2006, respectively.

She spent one year with the Friedrich-Alexander University of Erlangen–Nuremberg, Erlangen, Germany, and was with the Fraunhofer Institute for Integrated Circuits, Erlangen. From 2002 to 2007, she was with the Antenna Group, TNO Defence, Security and Safety Institute, The Hague, The Netherlands, initially a Ph.D. student and then as a Researcher. From 2007 to 2010, she was a Postdoctoral Fellow with the California Institute of Technology, working with the Sub Millimeter Wave Advance Technology Group, Jet Propulsion Laboratory, Pasadena, CA, USA. From 2010 to 2012, she was a Ramón y Cajal Fellow with the Optics Department, Complutense University of Madrid, Madrid, Spain. In September 2012, she joined the THz Sensing Group, Technical University of Delft, Delft, The Netherlands, where she is currently an Associate Professor. She has co-authored more than 150 journal and international conference contributions. Her research interests include the analysis and design of planar antennas, periodic structures, reflector antennas, lens antennas, and waveguide structures with an emphasis on the THz range.

Dr. Llombart was the recipient of the H. A. Wheeler Award for the Best Applications Paper of 2008 of the IEEE TRANSACTIONS ON ANTENNAS AND PROPAGATION, the 2014 THz Science and Technology Best Paper Award of the IEEE Microwave Theory and Techniques Society, and several NASA awards. She was also the recipient of the 2014 IEEE Antenna and Propagation Society Lot Shafai Mid-Career Distinguished Achievement Award. She serves as a Board member of the IRMMW-THz International Society. In 2015, she was a recipient of a European Research Council Starting Grant.